ARMA 18-1094

Modeling of rock inhomogeneity and anisotropy by explicit and implicit representation of microcracks

Abedi, R., Clarke, P.L.
Department of Mechanical, Aerospace & Biomedical Engineering, The University of Tennessee Space Institute, TN, USA

ABSTRACT: Fracture patterns experienced under a dynamic uniaxial compressive load are highly sensitive to rock microstructural defects due to its brittleness and the absence of macroscopic stress concentration points. We propose two different approaches for modeling rock microstructural defects and inhomogeneity. In the *explicit realization* approach, microcracks with certain statistics are incorporated in the computational domain. In the *implicit realization* approach, fracture strength values are sampled using a Weibull probability distribution. We use the Mohr-Coulomb failure criterion to define an effective stress in the context of an interfacial damage model. This model predicts crack propagation at angles $\pm\phi_{ch} = \pm(45 - \phi/2)$ relative to the direction of compressive load, where ϕ is the friction angle. By using appropriate models for fracture strength anisotropy, we demonstrate the interaction of rock weakest plane and ϕ_{ch}. Numerical results demonstrate the greater effect of strength anisotropy on fracture pattern when an explicit approach is employed. In addition, the density of fractures increases as the angle of the weakest planes approaches $\pm\phi_{ch}$. The fracture simulations are performed by an h-adaptive asynchronous spacetime discontinuous Galerkin (aSDG) method that can accommodate crack propagation in any directions.

Acknowledgments: The authors gratefully acknowledge partial support for this work via the U.S. National Science Foundation (NSF), CMMI - Mechanics of Materials and Structures (MoMS) program grant number 1538332 and CCF - Scalable Parallelism in the Extreme (SPX) program grant number 1725555.

1 INTRODUCTION

Heterogeneities in elastic properties and fracture strength can be either *explicitly* or *implicitly* incorporated in rock mechanics. In *explicit* approaches defects, microcracks, and other inhomogeneities are directly incorporated in the model. For example, in lattice models, the bulk is represented as a network of particles connected by springs. The inhomogeneity can be readily incorporated in lattice models by sampling the strength of springs from an assumed probability distribution [1,2]. For *Finite Element Methods* (FEMs), the explicit modeling of defects such as microcracks often requires a considerably finer discrete grid to capture the geometries of the defects. This in turn can substantially increase the computational cost. *Discrete Element Method* (DEM) and *peridynamics* methods model the media as a collection of interacting particles. Similar to lattice models, the material inhomogeneity can be *explicitly* modeled by assigning different bond stiffness between the particles. Some hybrid methods such as combined finite-discrete element method (FDEM) [3], have been proposed to combine the computational advantages of the FEMs and flexibility of discrete methods in modeling inhomogeneity. For example, [4,5] represents cracked regions by discrete elements while the intact parts are discretized by finite elements.

While accurate, explicit approaches can become quite expensive if defects of all sizes are directly incorporated in the computational model. The *implicit* approaches only include the collective effect of microstructures in macroscopic material models. Homogenization approaches derive macroscopic properties such as elastic moduli by solving the underlying problem in a *Volume Element* (VE). Similar approaches can also be used to calibrate continuum damage models, see for example [6–9]. For a macroscopically homogeneous material, the derived values converge to a unique value as the VE size approaches the size of the *Representative Volume Element* (RVE)—referred to as *Representative Elementary Volume* (REV) in rock mechanics. However, by using RVEs the statistical variations of properties from sample to sample, and spatial inhomogeneities of the material are lost. As an alternative, *Statistical Volume Elements* (SVEs), such as those in [10], use small enough VEs that such variations are preserved. Finally, phenomenological models attempt to represent material inhomogeneity and statistical variation without formally homogenizing it properties. The Weibull model [11,12], is one of such models that can provide an accurate representation of statistical nature of fracture strength of brittle materials such as rock.

Beside the higher accuracy and fidelity offered by explicit approaches, there are certain applications where defects such as cracks are preferred to be represented explicitly. For example, explicit representation of cracks greatly simplifies the application of hydraulic load on crack surfaces as opposed to complex thermodynamic formulations needed when cracks are implicitly modeled by a phase field fracture model [13] or other similar approaches. Moreover, the necessity of an explicit approach magnifies when the interaction of hydraulically loaded with in-situ cracks is considered [14]. In §5 as a future work, we proposed a *hybrid* approach that would combine the advantages of both explicit and implicit approaches.

In [15, 16], it is shown that incorporating material inhomogeneity plays an important role in predicting realistic fracture patterns. For rock, material anisotropy also plays a crucial rule; the existence of bedding planes not only affects the elastic properties, but also makes the rock weaker parallel to these planes; that is when the tensile load is normal to the direction of bedding planes. There are two main approaches to model the anisotropy of rock fracture properties. In [17, 18], a failure criterion is expressed in terms of invariants of stress tensor and a second order so-called microstructure tensor. While based on sound continuum mechanics theories, it is not straightforward to extract the fracture strength of rock for a given direction. In the second approach, typical failure criteria such as Mohr-Coulomb or Hoek-Brown are generalized such that for each direction, the parameters of these models are angle dependent; see for example [19].

We propose two approaches to model rock heterogeneities. In the *explicit realization* approach, we use certain statistics for microcrack density, location, and length to generate random realizations that contain a large number of microcracks. In the *implicit realization* approach, rather than using SVEs to homogenize effective properties, we use the phenomenological Weibull model to sample fracture strength values at the vertices of a discrete finite element mesh. As for modeling rock anisotropy, we adopt the second general approach described above for implicit realizations, in that the parameters of a failure criterion (Mohr-Coulomb) are angle dependent. For explicit realizations, the realized cracks are heavily oriented around a given angle. The problem specifically studied is the fracture of rock under dynamic uniaxial compressive load. For an isotropic model, the friction angle of rock dictates a preferable angle for the formation of cracks. However, when anisotropy is included, the competition of the natural angle of fracture under compressive load and the angle corresponding to weakest plane results in interesting fracture patterns for both explicit and implicit methods. The underlying elastodynamic problem is solved by an h-adaptive *asynchronous Spacetime Discontinuous Galerkin* (aSDG) method [20–22]. The fracture is modeled using an interfacial damage model [23]. A brief overview of the contact/fracture models and certain extensions for modeling anisotropic fracture based on Mohr Coulomb failure criterion are presented in the next two sections. Finally, §4 the effect of fracture strength anisotropy is studied for a problem where rock is under compressive dynamic load.

2 A RATE-DEPENDENT INTERFACIAL DAMAGE MODEL

This section provides an overview of the damage model presented in [23]. One difference will be the use of an effective stress model that is appropriate for the compressive mode fracture analysis presented in §4.

Instead of a traditional cohesive model, we present an interfacial damage model to represent fracture and contact modes on a crack surface. A scalar damage parameter, D, is used to interpolate between fully bonded ($D = 0$) and debonded ($D = 1$) states of an interface. It should be noted that in the majority of damage formulations, the stiffness of the bulk is degraded by the damage value. However, in our formulation, the damage model degrades the state on an interface. The contact modes include contact–stick and contact–slip modes as described in [24] as well as a separation mode which corresponds to fracture or crack opening. The use of Riemann solutions ensures that correct interface kinematic compatibility conditions are satisfied without resorting to penalty methods that are often combined with traditional cohesive models.

The formulation of traction and velocity values on a fracture section is comprised for two stages: First, the solutions within each of the three contact modes are presented in §2.1. Second, by using interpolation values such as D interface traction and velocity are obtained by forming a weighted average of individual contact mode solutions. This is described in §2.2. Finally, an effective stress model for fracture under compressive stress is presented in §2.3.

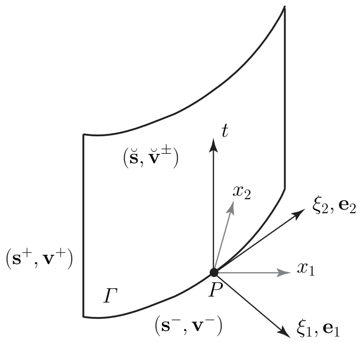

Figure 1: Local coordinate frame at an arbitrary location P on a spacetime fracture surface Γ.

2.1 *Riemann Contact Solutions*

Figure 1 shows a local coordinate system at an arbitrary location P on contact interface Γ in spacetime. The local coordinate (ξ_1, ξ_2, t) is chosen such that ξ_1-direction is normal to Γ. The quantities from opposite sides of Γ, decorated with superscripts + and −, define the initial data for the Riemann problem. Distinct velocity traces, $\mathbf{v}^{\pm}$, and tractions, $\mathbf{s}^{\pm}$, defined by $\mathbf{s} = \boldsymbol{\sigma} \cdot \mathbf{n}$ in which the same spatial normal vector, $\mathbf{n}$, is used to compute $\mathbf{s}^+$ and $\mathbf{s}^-$ from the traces of the stress tensor field on the interface, $\boldsymbol{\sigma}^{\pm}$. The Riemann solutions include the traction vector $\breve{\mathbf{s}}$

and velocity vectors $\breve{\mathbf{v}}^{\pm}$ that act on the interface. The Riemann solutions are obtained by preserving the characteristic values of the elastodynamic problem on each sides of the fracture interface and enforcing the appropriate type of kinematic compatibility (relation between $\breve{\mathbf{v}}^{+} = \breve{\mathbf{v}}^{-}$) for each type of contact solution. The Riemann solutions depend on material impedance values from the two sides ±,

$$Z^{i\pm} := \begin{cases} (c_d \rho)^{\pm} & i = 1 \\ (c_s \rho)^{\pm} & i = 2, 3 \end{cases} \tag{1}$$

in which the index i corresponds to spatial directions in the local frame shown in fig. 1 and the longitudinal and shear wave speeds are given by,

$$c_{\mathrm{d}} = \sqrt{\frac{\lambda + 2\mu}{\rho}}, \qquad c_{\mathrm{s}} = \sqrt{\frac{\mu}{\rho}}. \tag{2}$$

where ρ is mass density and λ, μ are Lamé parameters.

The Riemann solutions for contact–stick and bonded modes, decorated with subscripts ST and B respectively, are

$$\breve{s}^{i}_{\mathrm{B}} = \breve{s}^{i}_{\mathrm{ST}} = \breve{s}^{i} = \frac{s^{i+} Z^{i-} + s^{i-} Z^{i+}}{Z^{i-} + Z^{i+}} + \frac{Z^{i-} Z^{i+}}{Z^{i-} + Z^{i+}} (v^{+}_{i} - v^{-}_{i}) \tag{3a}$$

$$\breve{v}^{\mathrm{B}}_{i} = \breve{v}^{\mathrm{ST}}_{i} = \breve{v}_{i} = \frac{s^{i-} - s^{i+}}{Z^{i-} + Z^{i+}} + \frac{v^{+}_{i} Z^{i+} + v^{-}_{i} Z^{i-}}{Z^{i-} + Z^{i+}} \tag{3b}$$

In separation mode, $\breve{\mathbf{v}}^{+}$ and $\breve{\mathbf{v}}^{-}$ are independent. The target tractions are, however, set to $\mathbf{S}$, which in particular is obtained by the particular fracture model used at the interface. Similar to [15] we set $\mathbf{S} = \mathbf{0}$. The Riemann solutions for the separation case, decorated by S, are,

$$\breve{s}^{i}_{\mathrm{S}} = \breve{s}^{i} = S^{i} \tag{4a}$$

$$\breve{v}^{\mathrm{S}^{\pm}}_{i} = \breve{v}^{\pm}_{i} = v^{\pm}_{i} \pm \frac{S^{i} - s^{i\pm}}{Z^{i\pm}} \tag{4b}$$

In contact mode, a friction model determines which of the two contact–stick or contact–slip modes holds. This requires the definition of the *magnitude of tangential traction for bonded Riemann solutions* as,

$$\breve{\tau}_{\mathrm{B}} := \begin{cases} \sqrt{\left(\breve{s}^{2}_{\mathrm{B}}\right)^{2} + \left(\breve{s}^{3}_{\mathrm{B}}\right)^{2}} & d = 3 \\ |\breve{s}^{2}_{\mathrm{B}}| & d = 2 \end{cases} \tag{5}$$

where d is the spatial dimension. For the transition between contact–stick and contact–slip modes we use the Mohr–Coulomb friction law, which states that contact–slip mode holds if,

$$|\breve{\tau}_{\mathrm{B}}| > k \left\langle -\breve{s}^{1}_{\mathrm{B}} \right\rangle_{+} \tag{6}$$

in which k is the friction coefficient and $\langle . \rangle_{+}$ is the positive operator. Under these conditions, the magnitude of target shear traction is given by $k \left\langle -\breve{s}^{1}_{\mathrm{B}} \right\rangle_{+}$. The normal component of the traction and velocity vectors are enforced using the bonded Riemann solutions Eq. (3) (for $i = 1$) and the tangential velocities are obtained by preserving the characteristic values in directions $i \neq 1$ and using Mohr-Coulomb model for the tangential traction. For brevity, these solutions are not presented here and can be found in [24].

2.2 *Macroscopic Target Values*

The macroscopic, *i.e.,* averaged, solutions on Γ are obtained by interpolating between *bonded* and *debonded* solutions, using the damage parameter D,

$$\mathbf{s}^{*} := (1 - D)\breve{\mathbf{s}}_{B} + D\breve{\mathbf{s}}_{D} \tag{7a}$$

$$\mathbf{v}^{*\pm} := (1 - D)\breve{\mathbf{v}}_{B} + D\breve{\mathbf{v}}^{\pm}_{D} \tag{7b}$$

in which subscripts B and D denote Riemann values for bonded and debonded conditions.

The bonded solutions ($\breve{\mathbf{s}}_{B}$, $\breve{\mathbf{v}}_{B}$) are obtained from Eq. (3), while any of the separation, contact–stick, or contact-slip solutions can hold for the debonded values $\breve{\mathbf{s}}_{D}, \breve{\mathbf{v}}^{\pm}_{D}$. First, it should be determined whether the debonded part is in contact or separation model. Separation mode holds if the normal bonded traction $\breve{s}^{1}_{\mathrm{B}}$ is positive or the normal displacement jump is positive at P on Γ. Physically, the separation to contact mode transition is nonsmooth. Hence, a regularization scheme is proposed in [24] where the *relative contact fraction* transitions debonded solutions from complete separated values at $\eta = 0$ to full contact values at $\eta = 1$. On the other hand, [24] shows that stick to slip transitions are in fact smooth. Thus, the binary state *relative stick fraction*, $\gamma \in \{0, 1\}$ is used to transition between contact–stick ($\gamma = 1$) and contact–slip ($\gamma = 0$) modes. The Mohr–Coulomb condition Eq. (6) is used to determine whether stick or slip conditions hold.

In summary, $\breve{\mathbf{s}}_{D}$ and $\breve{\mathbf{v}}^{\pm}_{D}$ are interpolations of separation solutions Eq. (4), bonded/contact–stick solutions Eq. (3), and contact–slip [24] solutions. Considering the three relative fractions, D, η, and γ, it is easy to show that $\mathbf{s}^{*}$ and $\mathbf{v}^{*\pm}$ in Eq. (7) can be expressed as linear sums of the Riemann solutions from three distinct response modes, bonded/contact–stick (B), contact–slip (SL), and separation (S):

$$\mathbf{s}^{*} := a_{\mathrm{B}}\breve{\mathbf{s}}_{\mathrm{B}} + a_{\mathrm{SL}}\breve{\mathbf{s}}_{\mathrm{SL}} + a_{\mathrm{S}}\breve{\mathbf{s}}_{\mathrm{S}} \tag{8a}$$

$$\mathbf{v}^{*\pm} := a_{\mathrm{B}}\breve{\mathbf{v}}_{\mathrm{B}} + a_{\mathrm{SL}}\breve{\mathbf{v}}^{\pm}_{\mathrm{SL}} + a_{\mathrm{S}}\breve{\mathbf{v}}^{\pm}_{\mathrm{S}} \tag{8b}$$

with the coefficients

$$a_{\mathrm{B}} = 1 - D + D\eta\gamma \tag{9a}$$

$$a_{\mathrm{SL}} = D\eta(1 - \gamma) \tag{9b}$$

$$a_{\mathrm{S}} = D(1 - \eta) \tag{9c}$$

2.3 *Damage Evolution Law*

Bulk damage models that lack an intrinsic length scale, may result in non-convergent numerical solutions where damage localizes to layers whose width continues to shrink without limit as the mesh is refined [25, 26]. Similar problems exist for the interfacial damage models that lack a length scale. Instead of directly incorporating a length scale in the model, a length scale can be introduced through a time scale in the damage evolution law, as in [27] for a bulk model and [26, 28] for an interfacial model. We follow a similar approach and adopt the model in [29],

$$\dot{D} = \begin{cases} \frac{1}{\tau}[1 - H(\langle D_t - D \rangle)] & D < 1 \\ 0 & D = 1 \end{cases}, \tag{10}$$

in which $\tilde{\tau}$ is a *relaxation time*, and D_t is a *target damage value* that corresponds to the damage value under quasi-static loading conditions. The function H has unit value at zero and decreases to zero at infinity. Following [29], we use $H(x) = \exp(-ax)$. From the form of H, a maximum damage rate of $1/\tilde{\tau}$ is implied by Eq. (10).

In general, D_t depends on the states on both sides of the interface. We focus on a model where damage is mostly stress driven. In [23] we introduced a scalar *effective stress*, as $\breve{s} := \sqrt{\langle \breve{s}^1_{\mathrm{B}}\rangle^2 + (\beta \breve{\tau}_{\mathrm{B}})^2}$, where as in [30] β is the *shear stress factor*, and the positive operator, $\langle . \rangle$, ensures that no damage evolute incurs under compressive normal stress. There are two problems with this effective stress model. First, the shear strength of rock does not increase as the confinement pressure increases. Second, it predicts failure along ±45° for a uniaxial compressive test. As a result, in [31] we proposed an effective stress model that is based on Mohr-Coulomb failure criterion,

$$\breve{s} := \breve{\tau}_{\mathrm{B}} + k\breve{\sigma}^1_{\mathrm{B}} \tag{11}$$

where k is the friction coefficient introduced in Eq. (6). The *angle of friction* ϕ is defined as,

$$\phi = \tan^{-1}(k) \tag{12}$$

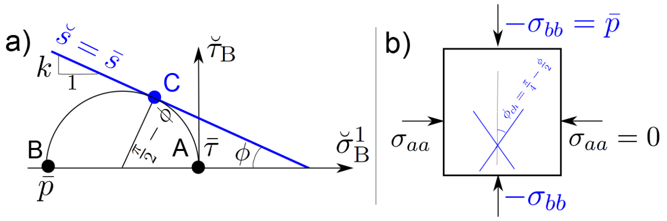

Figure 2: The compressive strength, $\bar{p}$, and the critical angle, ϕ_{ch}, for the Mohr–Coulomb model.

The condition $\breve{s} = \bar{s}$ corresponds to the Mohr-Coulomb *failure criterion* as shown in fig. 2a) and fracture strength based on Eq. (11) corresponds to cohesion, often denoted by c. This model also captures the correct compressive strength; as shown in fig. 2b), for a compressive loading scenario where σ_{bb} is set to the uniaxial compressive strength of rock $\bar{p}$, based on its corresponding stress state in 2a), for isotropic rock the value of $\bar{p}$ and the orientation of fracture plane with this load are determined as,

$$\bar{p} = 2\bar{\sigma}\frac{\cos(\phi)}{1-\sin(\phi)} = 2\bar{\sigma}\frac{1}{\sqrt{1+k^2}-k} \tag{13a}$$

$$\phi_{ch} = \pm\left(\frac{\pi}{4} - \frac{\phi}{2}\right) \tag{13b}$$

Once the effective stress is formulated based on the Mohr-Coulomb failure criterion, D_t is determined by,

$$D_t = \begin{cases} 0 & \breve{s} < \underline{s}, \\ \frac{\breve{s}-\underline{s}}{\bar{s}-\underline{s}} & \underline{s} \le \breve{s} < \bar{s}\ , \\ 1 & \bar{s} \le \breve{s} \end{cases} \tag{14}$$

where $0 < \underline{s} < \bar{s}$ are quasi-static strength thresholds for the initiation of damage evolution and complete failure, respectively. $\bar{s}$ is referred to as the *fracture strength*.

3 STATISTICAL ASPECTS

3.1 *Spatial Inhomogeneity*

In the explicit realization approach, microcracks are explicitly incorporated in the computational domain. The end points of these cracks are called *fracture surface tips* (FSTs) In the implicit realization approach, the effect of the in-situ defects can be homogenized to form an implicit representation of rock strength. In this approach, cracks can nucleation from points with lower strength and/or high stress values. In short, the tips of all active cracks in a computational domain, where pre-existed or nucleated afterward, is called a FST. In the aSDG method, used for the analyses in §4, cracks can only propagate from FSTs.

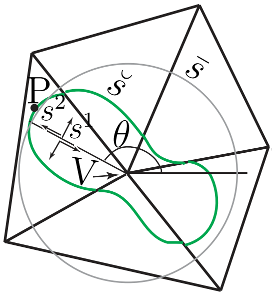

Figure 3: The angular distributions of effective stress $\breve{s}$ and fracture strength $\bar{s}$ around the FST V. The terms in Eq. (15) are $s^1 = \breve{\sigma}^1_{\mathrm{B}}$ and $s^2 = \breve{\tau}_{\mathrm{B}}$.

Figure 3 shows the distribution of $\breve{s}$ and $\bar{s}$ around the FSF V. The definition of effective for any arbitrary angle θ follows the definition Eq. (11) on fracture surfaces,

$$\breve{s}(\theta) := \breve{\tau}_{\mathrm{B}}(\theta) + k(\theta)\breve{\sigma}^1_{\mathrm{B}}(\theta) \tag{15}$$

A crack is extended for which the ratio $\breve{s}/\bar{s}$ is a local maximum with a value greater than or equal to unity Once a crack propagation direction is assigned to an FST, the underlying numerical method should accommodate an extension along the proposed direction. Unlike *eXtended finite element methods* (XFEMs) [32, 33] and *generalized finite element methods* (GFEMs) [34] where the underlying finite element mesh is not modified, mesh adaptive schemes, *e.g.,* [35, 36], move finite element vertices such that a finite element boundary is aligned with the proposed direction. Herein, we take the latter approach in that adaptive operations in spacetime can align element boundaries with any proposed crack propagation direction; *cf.* [23, 37] for more details. Once the crack is extended in the proposed direction, the vertex V becomes inactive and the new crack tip becomes an active FST.

3.1.1 *Explicit Realization*

In this method, the cracks are already included in the initial discretization. To generate the in-situ cracks, a certain statistics of cracks is assumed. Perhaps the most important statistics, the density of initial cracks is defined as,

$$\alpha = \frac{\sum_{i=1}^{\mathrm{nc}} l_i^2}{\mathrm{A}_c} \tag{16}$$

where l_i is the length of crack number i in a 2D domain with area A_c and nc is the number of cracks inside A_c. We assume the crack length to follow a Weibull distribution, and that their position in space to follow a uniform distribution. We use the "take and place" approach to sample and insert one crack in the computational domain at a time, until the target crack density is reached.

3.1.2 *Implicit Realization*

Incorporating in-situ microcracks and defects of rock in a computational domain can result in very expensive simulations. Instead, one can implicitly consider the effect of cracks that are short enough to enable the application of homogenization theories. Instead of using SVEs to homogenize the properties of rock and derive their statistical distribution, we employ a phenomenological model for the fracture strength of rock. The Weibull model [11, 12] has proved to be an accurate statistical model for fracture strength of brittle and quasi-brittle materials. The *cumulative distribution function* (CDF) for $\bar{s}$ for a region with area A is,

$$P(\bar{s}) = 1 - e^{-\frac{\mathrm{A}}{A_0}\left(\frac{\bar{s} - s_{\min}}{s_0}\right)^m} \tag{17}$$

The model parameters are a strength scale s_0, minimum fracture strength $s_{\min}$, and the Weibull modulus m. A_0 is the area for which the Weibull parameters are calibrated.

The way in which Eq. (17) is used in a computational setting is as follows. For any vertex V in the computational domain, this CDF is used to sample a fracture strength $\bar{s}$. The value A is chosen as an area that is associated with the vertex. For example, in fig. 3, A is set to the total area of the 5 surrounding triangles.

3.2 *Anisotropy*

Material properties of rock, including fracture strength, can be highly anisotropic, for example due to the existence of bedding planes. Two different approaches are used to incorporate rock anisotropy for the explicit realization and implicit realization methods. In the explicit method, crack orientation is biased around certain angles instead of following a uniform distribution in the range $[0,\ \pi]$. For example, to model bedding planes around the angle $\theta_0 = 30°$ a uniform distribution $[\theta_0 - \Delta\theta/2, \theta_0 + \Delta\theta/2]$ may be considered for crack orientation, where $\Delta\theta$ is the span of the angles of cracks.

For the implicit approach, fracture strength is not only assumed to be a function of location, through material inhomogeneity, but also anisotropic. The first aspect, inhomogeneity, is addressed by sampling a location-dependent (and angle-independent) strength $\bar{s}(V)$, as described in §3.1.2. To model anisotropy, the strength is made angle-dependent with the relation,

$$\bar{s}(V, \theta) = \bar{s}(V) f(\theta) \tag{18}$$

where $f(\theta)$ is a modulation function. Modulation of the parameters of a fracture strength model is one of the approaches to incorporate rock anisotropy in the literature. For example, [38] and [39] modify the parameters of the Mohr-Coulomb and Hoek-Brown [40] models, respectively.

In the discrete setting, the function $f(\theta)$ is sampled separately for each vertex V of the discrete domain. The function $f(\theta)$ is characterized by θ_0 and f_0 the angle and minimum modulation of the function $f(\theta)$; that is $f(\theta)$ takes the minimum value of f_0 at $\theta_0 \pm \pi$. As discussed in §4, some randomness is incorporated in the sampling of f_0 and θ_0 for each vertex. Finally, once fracture strength is fully characterized by Eq. (18) for V at all angles θ, the direction of extension is determined as the angle that maximizes $\breve{s}(\theta)/\bar{s}(V, \theta)$. A propagation from V is not realized until this maximum ratio exceeds unity.

In conclusion, in the explicit realization approach, fracture strength is not inhomogeneous nor anisotropic. That is, a unique angle independent value is used for $\bar{s}$ in contrast to the model Eq. (18) for the implicit realization method. In addition, no cracks are permitted to nucleated inside the domain. These are consequences of the assumption that the random and explicit distribution of cracks is the only source of randomness for the explicit realization approach.

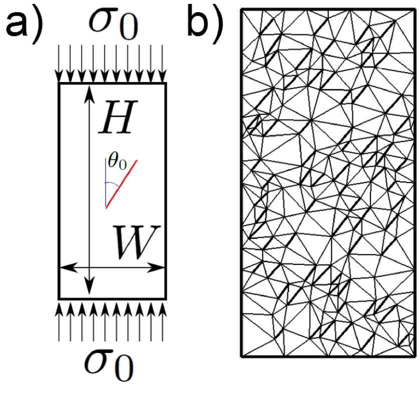

Figure 4: Compressive fracture of a rectangular domain: a) Domain geometry and loading; b) The discrete initial mesh for an explicit realization with $\alpha = 0.5$ and angular bias $\theta_0 = 40°$.

4 NUMERICAL RESULTS

Figure 4a) diagrams a problem involving compressive uniaxial loading applied to a rectangular domain in which the load ramps from zero to a sustained value of $\sigma_0 = 2.5$MPa

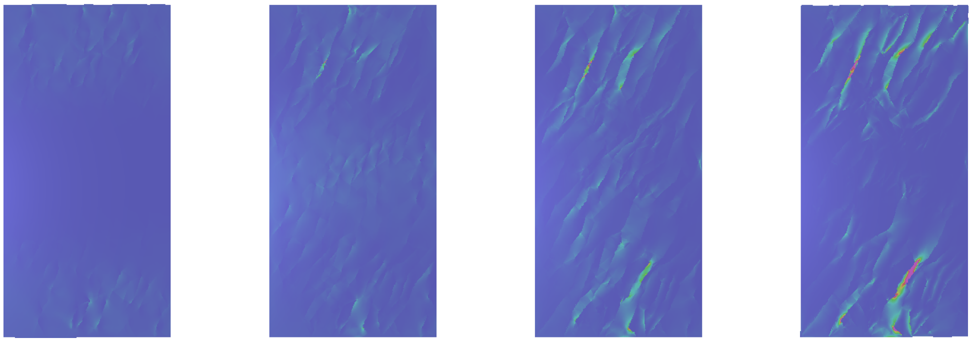

(a) $t = 14$ μs. (b) $t = 22$ μs. (c) $t = 30$ μs. (d) $t = 40$ μs.

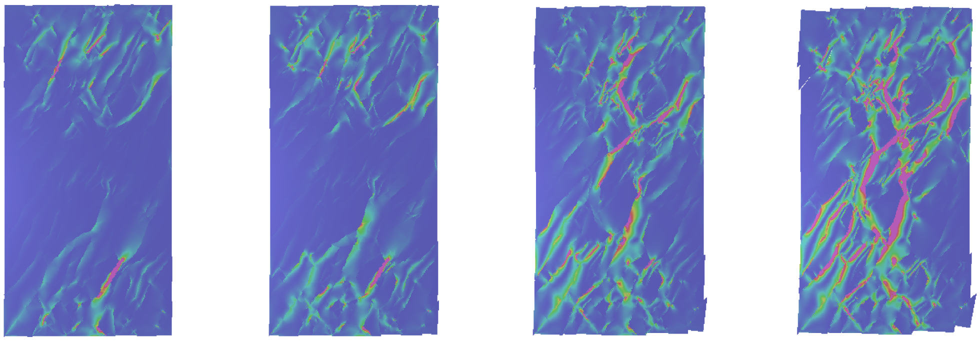

(e) $t = 50$ μs. (f) $t = 60$ μs. (g) $t = 80$ μs. (h) $t = 100$ μs.

Figure 5: A sequence of solutions for an explicit realization with $\alpha = 0.5$ and angular bias $\theta_0 = 20°$. Strain energy density is mapped to color with blue-to-red range indicating low to high values.

over 10 microseconds. The domain dimensions are $W = 0.08$ m and $H = 0.16$ m. The angle of weak planes for both implicit and explicit realizations with respect to the load direction (vertical direction) is denoted by θ_0 in the clockwise direction as shown. Similar to θ_0, all the angles are measured relative to the vertical direction in the clock-wise direction. The material properties are: Young's modulus $E = 65$ GPa, mass density $\rho = 2600$ kg/m^3, and Poisson's ratio $\nu = 0.27$. The friction coefficient is $k = 0.3$, corresponding to $\phi = 16.9°$. In the absence of fracture strength anisotropy we would expect cracks along $\pm\phi_{ch}$, where $\phi_{ch} = (45° - \phi/2) = 36.65°$;*cf.* Eq. (13b) and fig. 2b).

The two different explicit and implicit realization models are used for this study. Figure 4b) shows an explicit realization spatial mesh for crack density $\alpha = 0.5$. The realized microcrack orientations are sampled from a uniform distribution with the average angle $\theta_0 = 40°$ and a span of $\Delta\theta = 10°$. The fracture strength is set to $\bar{s} = 1.344$ MPa, which from Eq. (13a) yields a uniaxial fracture strength of $\bar{p} = 3.612$ MPa. Thus, in the absence of microcracks the compressive load of $\sigma_0 = 2.5$MPa is not large enough to cause any crack nucleation before the magnitude of the load doubles when the waves propagating from the top and bottom intersect in the middle of the domain. However, the presence of microcracks implies that cracks can propagate from their tips even under this applied load.

Figure 5 shows the solution visualization for an explicit realization with $\alpha = 0.5$ and mean microcrack angle $\theta_0 = 20°$; *cf.* fig. 4a). In the presence of microcracks, two things happen; first, between the two angles $\pm\phi_{ch} = \pm 36.65°$ the $+\phi_{ch}$ has a much closer direction to in-situ cracks. So, if there are long distances between cracks more cracks with the angle ϕ_{ch}, rather than $-\phi_{ch}$, are expected. Second, the microcrack directions to a large extend direct crack propagation directions as they create weak planes along the θ_0 direction. From the energy density visualizations in fig. 5 both expectations are verified. First, not many cracks are observed with negative angles with respect to the load direction. Second, the majority of cracks propagate along $\theta_0 = 20$ and its only between the cracks that angles closer to anticipated $\phi_{ch} = 36.65°$ connects the cracks. The competition between θ_0 and ϕ_{ch} and high stress concentrations in the fracture process zones around the crack tips and on the sides of the crack surfaces, due to frictional sliding, can clearly be seen in figs. 5(f-h).

Figure 6 compares the results for explicit realization simulations for different mean values of microcrack orientation θ_0. As mentioned, the natural angles of crack extension are along $\pm\phi_{ch} = \pm 36.65°$. In fig. 6a, the cracks are too close to vertical direction and their direction is not close to $\pm\phi_{ch}$, however, still ϕ_{ch} is closer to crack directions and more of this angle of crack propagation is expected between microcracks. The reorientation of propagating cracks in this direction can clearly be seen in the figure. This trend continues in fig. 6b but with slightly more straight path for cracks. Finally, in fig. 6c and especially fig. 6d, the angle of in-situ cracks gets so close to

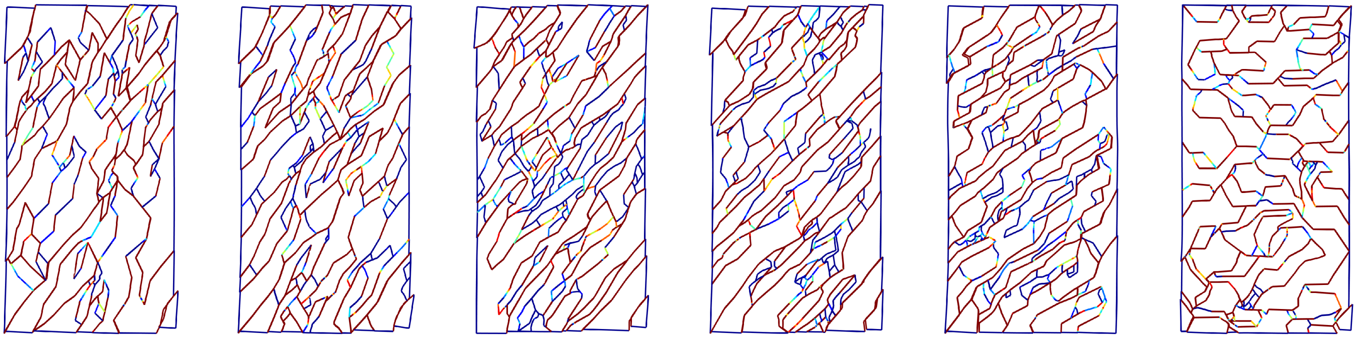

(a) $\theta_0 = 10°$. (b) $\theta_0 = 20°$. (c) $\theta_0 = 30°$. (d) $\theta_0 = 40°$. (e) $\theta_0 = 60°$. (f) $\theta_0 = 90°$.

Figure 6: Comparison of fracture patterns and deformed shapes for the explicit realization model for crack density $\alpha = 0.5$ and different values for angular bias θ_0 at time $t = 90$ μs. The crack segments are color coded with the damage value $D \in [0,\ 1]$ mapped to the blue to red color range.

ϕ_{ch} that first much more straight crack path is observed and second due to the energetically favorable propagation of cracks, a denser fracture network is observed. As the crack angles get farther away from ϕ_{ch} in fig. 6e, crack paths start to become more complex. Finally, for $\theta_0 = 90°$ in fig. 6f there is no preferred direction between $\pm\phi_{ch}$ and cracks with both directions are observed. In addition, the very unfavorable direction of microcracks greatly inhibits crack propagation under the compressive stress loading.

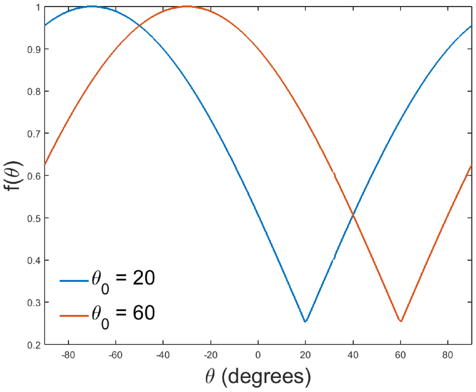

Figure 7: Sample $f(\theta)$ functions, *cf.* Eq. (18), for $f_0 = 0.25$ and $\theta_0 = 20°$ and $\theta_0 = 60°$.

Next, the results for the implicit approach are presented. Two aspects need to be addressed; first, the inhomogeneity of fracture strength is realized by sampling $\bar{s}$ from Eq. (17). The values $m = 4$, $s_{\min} = 0.74$ MPa, $s_0 = 2.69$ MPa, and $A_0 = 0.01$ m^2 imply a mean strength $\mathbb{E}(\bar{s}) = 3.03$ MPa for $A = W \times H = 0.0128$ m^2 in Eq. (17). This corresponds to a mean compressive strength of $\mathbb{E}(\bar{p}) = 8.14$ MPa which is significantly larger than the applied load $\sigma_0 = 2.5$MPa. However, the statistical variation of sampled $\bar{s}$ implies that for the points whose sampled compressive strength is smaller than $\sigma_0 = 2.5$MPa, a crack can be nucleated.

The anisotropy of the fracture strength is modeled by the function $f(\theta)$, *cf.* Eq. (18). For all the implicit realizations $f(\theta)$ ranges from one to its minimum value $f_0 = 0.25$ at an angle with ±5° variation around a specified angle θ_0. Figure 7 shows two samples for $f(\theta)$ for $\theta_0 = 20°$ and $\theta_0 = 60°$, where as shown in fig. 4 and evident in this figure, θ_0 and $\theta_0 \pm 90°$ correspond to the weakest and strongest planes.

A sequence of solutions for an implicit realization with angle bias $\theta_0 = 20°$ is shown in fig. 8. Comparing corresponding times in figs. 8(a-d) with those from explicit realization in figs. 5(a-d), we observe that fewer cracks are observed for the implicit approach. This is expected for the two particular set-ups considered, as in the explicit approach the large microcracks can greatly increase stress fields around the crack tips and cause further crack propagation. Also apparent in figs. 8(a-d) is that most cracks propagation along positive angles, which is expected by having weakest plane at $\theta_0 = 20°$. The results in figs. 8(e-h) show high level of compaction near the top and bottom boundaries. Also, while more cracks are observed close to θ_0 to ϕ_{ch}, see for example figs. 8(g-h), there are also cracks close to $-\phi_{ch}$. In comparison to fig. 5, we observe that the explicit representation of microcracks results in much more focused propagation of cracks in the range θ_0 to ϕ_{ch}.

Figure 9 compares fracture patterns for different angles of the weakest plane θ_0 for the implicit realization model. Similar to the explicit realization model, the highest density of cracks are observed when weakest planes are close to natural angle of fracture $\phi_{ch} = 36.65°$, that is for $\theta_0 = 30°$ and $\theta_0 = 40°$, in figs. 9(c-d). Moreover, unlike the explicit model, where the orientation of microcracks at positive angles heavily prevented crack propagation at negative angles, for the implicit model a considerable density of cracks can be observed at negative angles. However, by closer examination, the majority of cracks with substantial damage, red color, are in positive directions.

Finally, fig. 10 shows the finite element front meshes for the implicit realization approach for different angles θ_0 at a later time $t = 150$ μs. These figures demonstrate the level of mesh refinement and adaptivity close to the top and bottom boundaries that are caused by the compaction of rock. This is a testament to the aSDG methods powerful meshing operations that accommodate crack propaga-

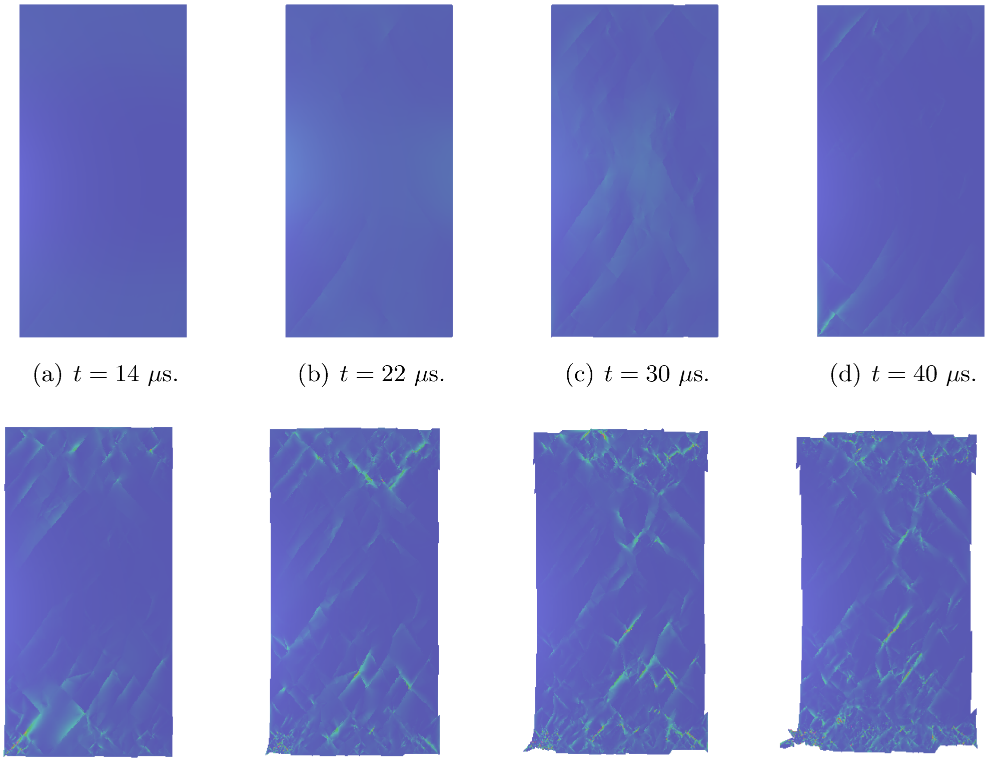

(a) $t = 14$ μs. (b) $t = 22$ μs. (c) $t = 30$ μs. (d) $t = 40$ μs.

(e) $t = 60$ μs. (f) $t = 80$ μs. (g) $t = 100$ μs. (h) $t = 120$ μs.

Figure 8: A sequence of solutions for an implicit realization with min stress ratio $f_0 = 0.25$ and angular bias $\theta_0 = 20°$. Strain energy density is mapped to color with blue-to-red range indicating low to high values.

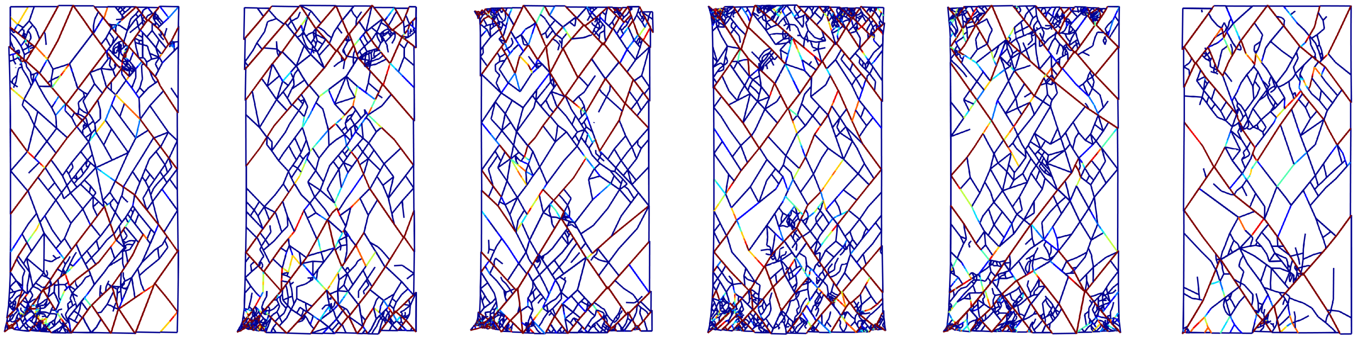

(a) $\theta_0 = 10°$. (b) $\theta_0 = 20°$. (c) $\theta_0 = 30°$. (d) $\theta_0 = 40°$. (e) $\theta_0 = 60°$. (f) $\theta_0 = 90°$.

Figure 9: Comparison of fracture patterns and deformed shapes for the implicit realization model for minimum strength factor $f_0 = 0.25$ and different values for angular bias θ_0 at time $t = 90$ μs. The crack segments are color coded with the damage value $D \in [0,\ 1]$ mapped to the blue to red color range.

tion in arbitrary directions. The map of a_{SL} to color also demonstrate which crack segments are in slip mode. As evident, at this time the majority of crack segments are in contact–stick mode. The local sliding of certain crack segments at different times is responsible for the deformed shapes observed in fig. 9.

5 CONCLUSIONS

We presented the explicit and implicit realization approaches to model rock inhomogeneity. Modeling of rock inhomogeneity is essential in problems that lack initial stress concentration points, such as rock fracture under axial compressive load studied in this manuscript. In addition, for this problem in an isotropic rock medium, cracks tend to nucleation and propagate along $\pm\phi_{ch} = \pm(45° - \phi/2)$ directions with respect to the compressive load direction. We studied the effect of rock anisotropy on the angles at which cracks propagate. It was demonstrated that in the explicit approach where the microcracks were directly incorporated in the computational domain, the angle of weakest plane of rock had a more major role

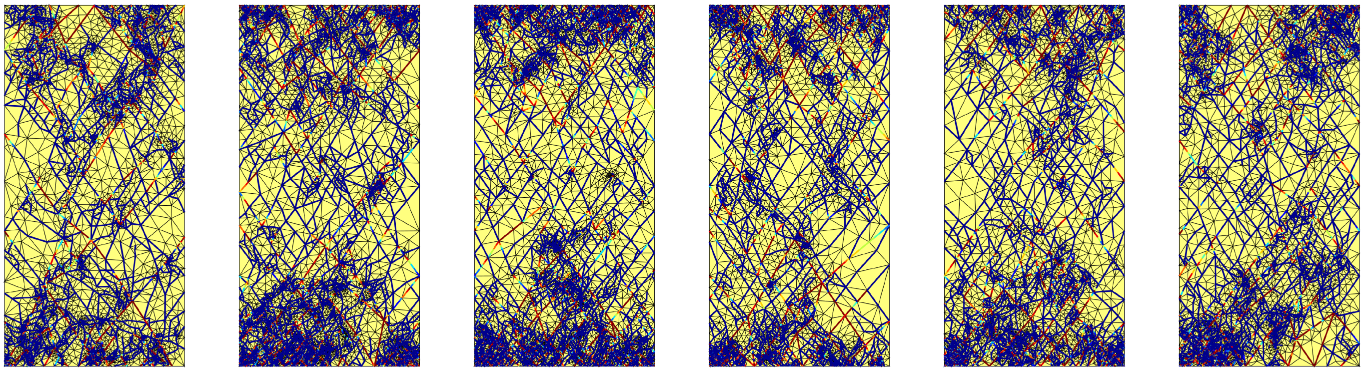

(a) $\theta_0 = 0°$. (b) $\theta_0 = 30°$. (c) $\theta_0 = 50°$. (d) $\theta_0 = 60°$. (e) $\theta_0 = 70°$. (f) $\theta_0 = 80°$.

Figure 10: Comparison of the front meshes and a_{SL} for the implicit realization model for minimum strength factor $f_0 = 0.25$ and different values for angular bias θ_0 at time $t = 150$ μs. The crack segments are color coded with $a_{\mathrm{SL}} \in [0,\ 1]$ mapped to the blue to red color range.

on fracture patterns. Moreover, for both approaches, more cracks propagated when the weakest plane direction tended to the natural fracture angle ϕ_{ch}.

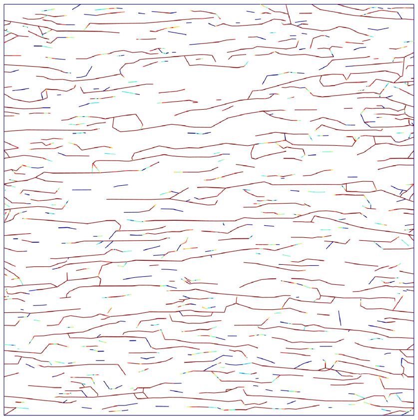

Figure 11: Fracture in isotropic rock under vertical uniaxial tensile stress.

In this manuscript, we only studied fracture in anisotropic rock under uniaxial compressive stress without side confinement. There are some other interesting fracture modes where anisotropy plays an important role. Figure 11 shows the fracture pattern in an unconfined rock specimen under a vertical uniaxial tensile loading. As observed, most fractures are perpendicular to the direction of tensile loading. It is worth mentioning that the original Mohr-Coulomb model used in this manuscript is not appropriate for this type of fracture analysis; *cf.* [31] for further discussion on the choice of fracture model. The second effect is the presence of lateral confinement for uniaxial compressive loading scenarios. Similar to the results presented herein, many experimental and numerical studies [41–46] show the appearance of diagonal cracks at angles $\pm(45° \pm \phi/2)$ relative to the direction of compressive loading for isotropic rock. Figure 12 shows the effect of confinement (on the left and right sides) on fracture pattern for a sample under vertical compressive loading. The appearance of more cracks along the (vertical) loading direction is contributed to the effect of stress confinement. In future work, we will investigate the effect of anisotropy on fracture pattern for other loading scenarios such as those shown in fig. 11 and fig. 12.

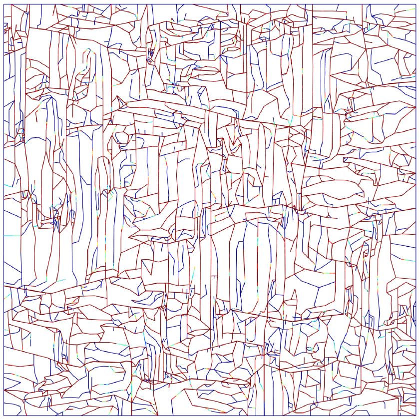

Figure 12: Fracture in isotropic rock under vertical uniaxial compressive stress with side confinement.

There are also other extensions to this study from a statistical perspective. First, the homogenization of SVEs, rather than using the phenomenological Weibull model, can greatly improve the accuracy of rock inhomogeneity with the implicit realization approach. Second, for explicit realization of crack actual microcrack statistics such as those reported in [47] and more robust approaches for their generation [48] can be employed. Third, for a more quantitative analysis quantities of interest such as maximum attainable compressive stress and dissipated fracture energy can be derived as a function loading rate and material inhomogeneity and anisotropy; as shown in [16, 49], modeling rock inhomogeneity becomes more important at higher loading rates and models that treat rock as a homogeneous medium greatly overestimate the induced density of cracks. Finally, while the explicit approach is more realistic, the computational cost prohibits its direct application to many practical problems. We plan to propose a *hybrid* approach that to some extend preserves the accuracy of an explicit approach and the efficiency of an implicit approach; cracks under a certain size will be *homogenized* to an *implicit* representation of strength, while longer cracks are *explicitly* modeled and are maintained in the problem description. This would unify the two types of analyses presented in this manuscript.

REFERENCES

[1] Schlangen, E. and E.J. Garboczi (1997) Fracture simulations of concrete using lattice models: Computational aspects. *Engineering Fracture Mechanics*, **57**, 319–332.

[2] Li, H.L., Y.L. Bai, M.F. Xia, F.J. Ke, and X.C. Yin (2000) Damage localization as a possible precursor of earthquake rupture. *pure and applied geophysics*, **157**, 1929–1943.

[3] Munjiza, A. (2004) *The combined finite-discrete element method*. Wiley.

[4] Mahabadi, OK, A Lisjak, A Munjiza, and G Grasselli (2012) Y-geo: New combined finite-discrete element numerical code for geomechanical applications. *International Journal of Geomechanics*, **12**, 676–688.

[5] Mahabadi, O.K., B.S.A. Tatone, and G. Grasselli (2014) Influence of microscale heterogeneity and microstructure on the tensile behavior of crystalline rocks. *Journal of Geophysical Research: Solid Earth*, **119**, 5324–5341.

[6] Taylor, Lee M., Er-Ping Chen, and Joel S. Kuszmaul (1986) Microcrack-induced damage accumulation in brittle rock under dynamic loading. *Computer Methods in Applied Mechanics and Engineering*, **55**, 301 – 320.

[7] Homand-Etienne, F., D. Hoxha, and J.F. Shao (1998) A continuum damage constitutive law for brittle rocks. *Computers and Geotechnics*, **22**, 135–151.

[8] Shao, J.F. and J.W. Rudnicki (2000) A microcrack-based continuous damage model for brittle geomaterials. *Mechanics of Materials*, **32**, 607–619.

[9] Lu, Y.L., D. Elsworth, and L.G. Wang (2013) Microcrack-based coupled damage and flow modeling of fracturing evolution in permeable brittle rocks. *Computers and Geotechnics*, **49**, 226–44.

[10] Koyama, Tomofumi and Lanru Jing (2007) Effects of model scale and particle size on micro-mechanical properties and failure processes of rocks—a particle mechanics approach. *Engineering Analysis with Boundary Elements*, **31**, 458–472.

[11] Weibull, W. (1939) A statistical theory of the strength of materials. *R. Swed. Inst. Eng. Res.*, p. Res. 151.

[12] Weibull, W. (1951) A statistical distribution function of wide applicability. *Journal of Applied Mechanics*, **18**, 293–297.

[13] Wilson, Zachary A. and Chad M. Landis (2016) Phase-field modeling of hydraulic fracture. *Journal of the Mechanics and Physics of Solids*, **96**, 264–90.

[14] Clarke, Philip L. and Reza Abedi Modeling the connectivity and intersection of hydraulically loaded cracks with in-situ fractures in rock. *International journal for numerical and analytical methods in geomechanics*, In Press.

[15] Clarke, P.L., R. Abedi, B. Bahmani, K.A. Acton, and S.C. Baxter (November 3-9, 2017) Effect of the spatial inhomogeneity of fracture strength on fracture pattern for quasi-brittle materials. *Proceedings of ASME 2017 International Mechanical Engineering Congress & Exposition IMECE 2017*, Tampa, Florida, USA, IMECE2017-71515, 11 pages.

[16] Abedi, R., O. Omidi, and P.L. Clarke (June 25-28, 2017) A numerical study on the effect of loading and randomness on fracture patterns in a tight formation. *Proceeding: 51th US Rock Mechanics/Geomechanics Symposium*, San Francisco, California, USA, ARMA 17-0641 (12 pages).

[17] Pietruszczak, S. and Z. Mroz (2000) Formulation of anisotropic failure criteria incorporating a microstructure tensor. *Computers and Geotechnics*, **26**, 105–112.

[18] Pietruszczak, S., D. Lydzba, and J.F. Shao (2002) Modelling of inherent anisotropy in sedimentary rocks. *International Journal of Solids and Structures*, **39**, 637–648.

[19] Shi, Xiangchao, Xu Yang, Yingfeng Meng, and Gao Li (2016) An anisotropic strength model for layered rocks considering planes of weakness. *Rock Mechanics and Rock Engineering*, **49**, 3783–92.

[20] Abedi, Reza, Robert B. Haber, and Boris Petracovici (2006) A spacetime discontinuous Galerkin method for elastodynamics with element-level balance of linear momentum. *Computer Methods in Applied Mechanics and Engineering*, **195**, 3247–73.

[21] Abedi, R., R. B. Haber, S. Thite, and J. Erickson (2006) An h–adaptive spacetime–discontinuous Galerkin method for linearized elastodynamics. *Revue Européenne de Mécanique Numérique (European Journal of Computational Mechanics)*, **15**, 619–42.

[22] Abedi, R (2016) A comparative and parametric study of dynamic cohesive and linear elastic fracture mechanics models. *International Journal of Solids and Structures*, **102**, 163–175.

[23] Abedi, Reza, Robert B. Haber, and Philip L. Clarke (2017) Effect of random defects on dynamic fracture in quasi-brittle materials. *International Journal of Fracture*, **208**, 241–268.

[24] Abedi, Reza and Robert B. Haber (2014) Riemann solutions and spacetime discontinuous Galerkin method for linear elastodynamic contact. *Computer Methods in Applied Mechanics and Engineering*, **270**, 150–77.

[25] Bazant, Zdenek P., Ted B. Belytschko, and Ta-Peng Chang (1984) Continuum theory for strain-softening. *Journal of Engineering Mechanics*, **110**, 1666–1692.

[26] Allix, O., P. Feissel, and P. Thevenet (2003) A delay damage mesomodel of laminates under dynamic loading: basic aspects and identification issues. *Computers and Structures*, **81**, 1177–1191.

[27] Needleman, A. (1988) Material rate dependence and mesh sensitivity in localization problems. *Computer Methods in Applied Mechanics and Engineering*, **67**, 69–85.

[28] Corigliano, A and M Ricci (2001) Rate-dependent interface models: formulation and numerical applications. *International Journal of Solids and Structures*, **38**, 547–576.

[29] Allix, O and A Corigliano (1999) Modeling and simulation of crack propagation in mixed-modes interlaminar fracture specimens. *International Journal of Fracture*, **38**, 111–140.

[30] Camacho, G. T. and M. Ortiz (1996) Computational modelling of impact damage in brittle materials. *International Journal of Solids and Structures*, **33**, 2899–2938.

[31] Abedi, R., R.B. Haber, and A. Elbanna (June 25-28, 2017) Mixed-mode dynamic crack propagation in rocks with contact-separation mode transitions. *Proceeding: 51th US Rock Mechanics/Geomechanics Symposium*, San Francisco, California, USA, ARMA 17-0679 (12 pages).

[32] Belytschko, T. and T. Black (1999) Elastic crack growth in finite elements with minimal remeshing. *International Journal for Numerical Methods in Engineering*, **45**, 601–620.

[33] Moes, N., J. Dolbow, and T. Belytschko (1999) A finite element method for crack growth without remeshing. *International Journal for Numerical Methods in Engineering*, **46**, 131–150.

[34] Strouboulis, T., K. Copps, and I. Babuška (2001) The generalized finite element method. *Computer Methods in Applied Mechanics and Engineering*, **190**, 4081–4193.

[35] Rangarajan, Ramsharan and Adrian J Lew (2014) Universal meshes: A method for triangulating planar curved domains immersed in nonconforming meshes. *International Journal for Numerical Methods in Engineering*, **98**, 236–264.

[36] Rangarajan, Ramsharan, Maurizio M Chiaramonte, Michael J Hunsweck, Yongxing Shen, and Adrian J Lew (2015) Simulating curvilinear crack propagation in two dimensions with universal meshes. *International Journal for Numerical Methods in Engineering*, **102**, 632–670.

[37] Omidi, Omid, Reza Abedi, and Saeid Enayatpour (June 28-July 1, 2015) An adaptive meshing approach to capture hydraulic fracturing. *The 49th US Rock Mechanics/Geomechanics Symposium*, San Francisco, California, USA, ARMA 15-572 (9 pages).

[38] Pietruszczak, S. and Z. Mroz (2001) On failure criteria for anisotropic cohesive-frictional materials. *International Journal for Numerical and Analytical Methods in Geomechanics*, **25**, 509–524.

[39] Lee, Y.-K. and S. Pietruszczak (2008) Application of critical plane approach to the prediction of strength anisotropy in transversely isotropic rock masses. *International Journal of Rock Mechanics and Mining Sciences*, **45**, 513–23.

[40] Hoek, E. and T. Brown (1980) *Underground Excavations in Rock*. Geotechnics and foundations, Taylor & Francis.

[41] Tang, CA, LG Tham, PKK Lee, Y Tsui, and H Liu (2000) Numerical studies of the influence of microstructure on rock failure in uniaxial compression - part II: constraint, slenderness, and size effect. *International Journal of Rock Mechanics and Mining Sciences*, **37**, 571–583.

[42] Teng, JG, WC Zhu, and CA Tang (2004) Mesomechanical model for concrete. part II: applications. *Magazine of Concrete Research*, **56**, 331–345.

[43] Li, Gen and Chun-An Tang (2015) A statistical meso-damage mechanical method for modeling trans-scale progressive failure process of rock. *International Journal of Rock Mechanics and Mining Sciences*, **74**, 133–150.

[44] Dinç, Özge and Luc Scholtès (2017) Discrete analysis of damage and shear banding in argillaceous rocks. *Rock Mechanics and Rock Engineering*, pp. 1–18.

[45] Bahmani, Bahador, Philip L. Clarke, and Reza Abedi (2018) A bulk damage model for modeling dynamic fracture in rock. *Proceeding: 52nd US Rock Mechanics/Geomechanics Symposium*, Seattle, Washington, USA, ARMA 18-151-0228-0826 (9 pages).

[46] Rangari, Sachin, K Murali, and Arghya Deb (2018) Effect of meso-structure on strength and size effect in concrete under compression. *Engineering Fracture Mechanics*.

[47] Olarewaju, Joseph, Saleem Ghori, Alhasan Fuseni, Mohammed Wajid, et al. (1997) Stochastic simulation of fracture density for permeability field estimation. *Middle East Oil Show and Conference*, Society of Petroleum Engineers.

[48] Huq, F., R. Brannon, and L. Graham-Brady (2016) An efficient binning scheme with application to statistical crack mechanics. *International Journal for Numerical Methods in Engineering*, **105**, 33–62.

[49] Omidi, Omid, Reza Abedi, and Saeid Enayatpour (June 26-29, 2016) Well stimulation in tight formations: a dynamic approach. *Proceeding: 50th US Rock Mechanics/Geomechanics Symposium*, Houston, Texas, USA, ARMA 16-0150 (12 pages).